Electronic Supplementary Material (ESI) for Sustainable Energy & Fuels.

A Manganese Complex on a Gas Diffusion Electrode for Selective CO_2 to CO Reduction

Catherine Eagle,[1] Gaia Neri,[1,2] Verity L. Piercy,[1,3] Khadija Younis,[1] Bhavin Siritanaratkul,[1] Alexander J. Cowan[1]*

*acowan@liverpool.ac.uk

[1]Stephenson Institute for Renewable Energy and the Department of Chemistry, University of Liverpool, Liverpool, L69 7ZF

[2] Current address, Enapter, Pisa, Tuscany, Italy

[3] Current address, NSG Pilkington, Latham, Ormskirk, UK

1. Characterisation of the Mnbpy GDE

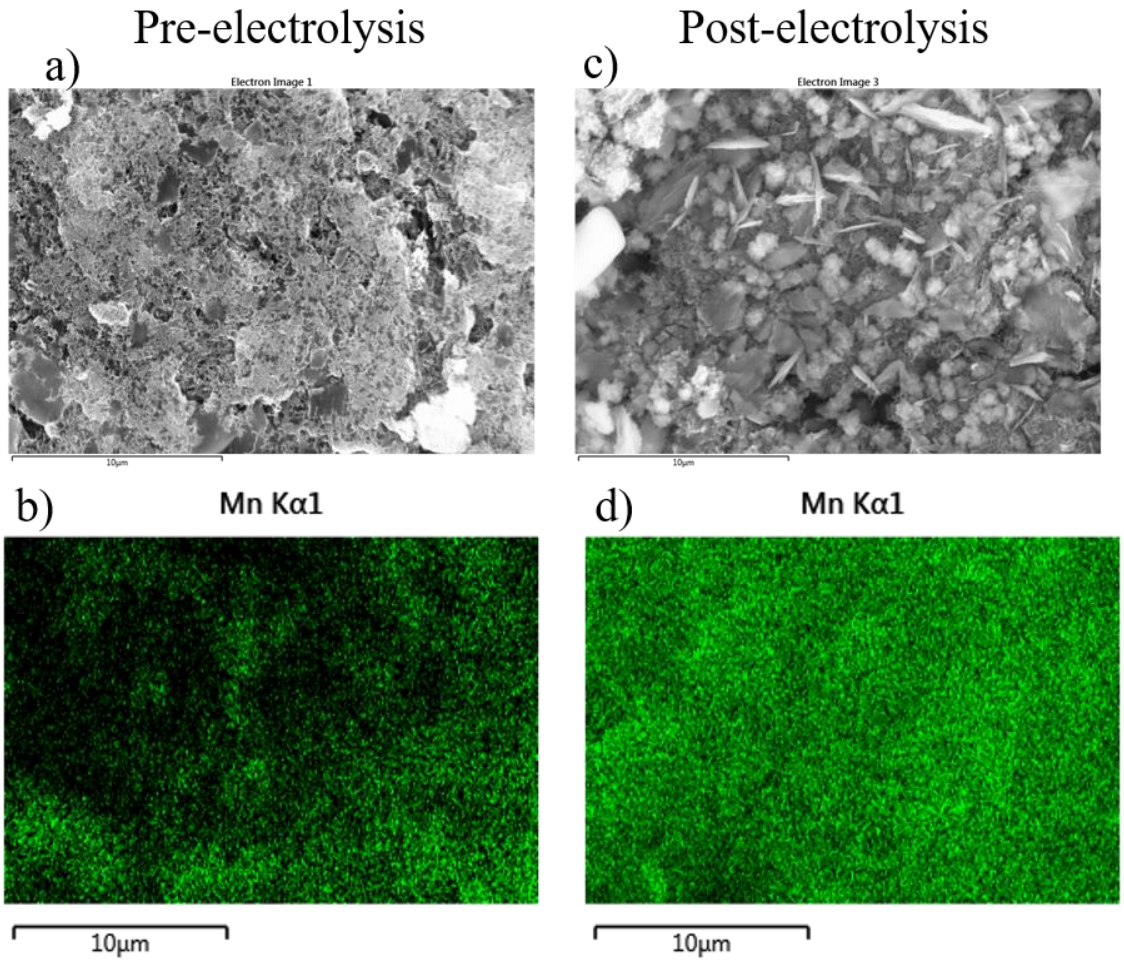

Figure S1: SEM-EDX mapping of GDE prepared using Mnbpy with MWCNT on carbon cloth, pre (a,b) and post (c,d) 12-hour electrolysis at -0.98 V_{RHE} in the flow cell using a 0.5 M $KHCO_3$ electrolyte.

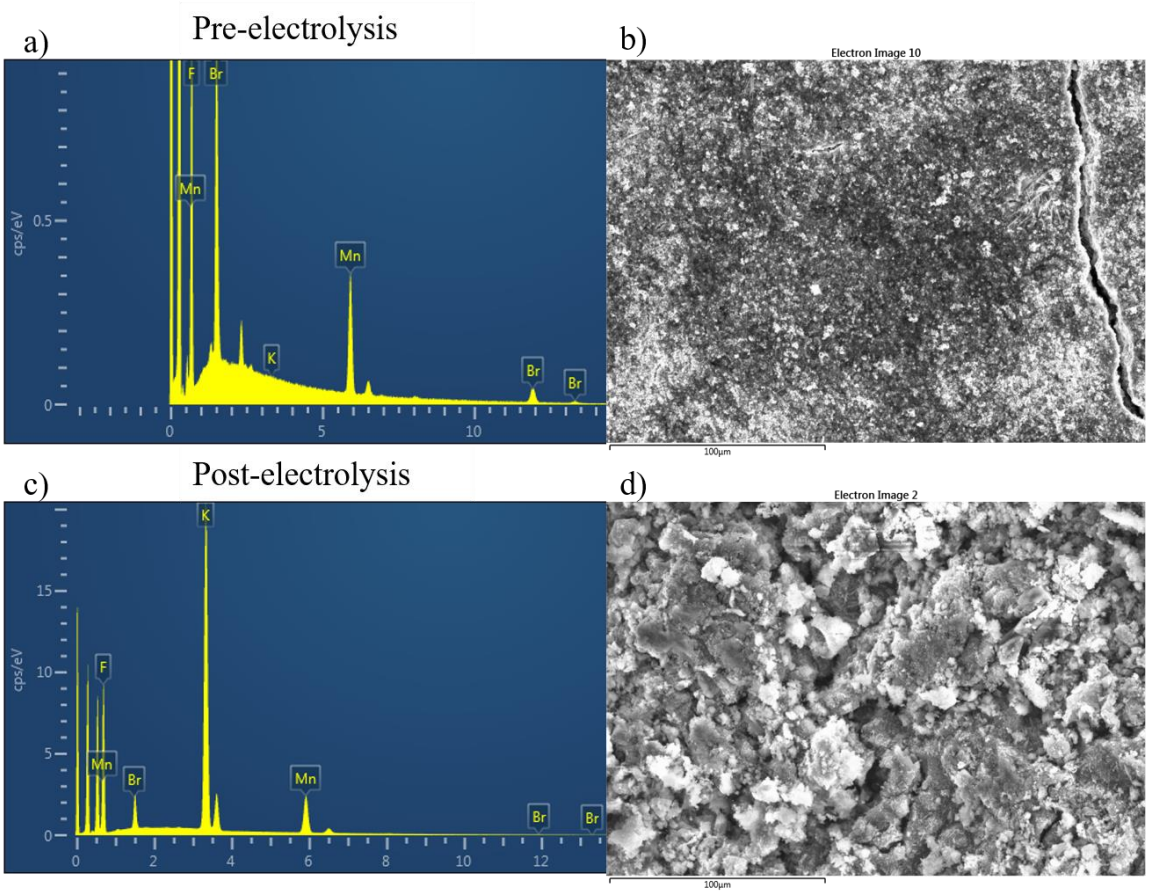

Figure S2: SEM-EDX mapping of GDE prepared using Mnbpy with MWCNT on carbon paper, pre- (a,b) and post- (c,d) electrolysis in a zero-gap cell with BPM at -50 mA cm^{-2} for two hours.

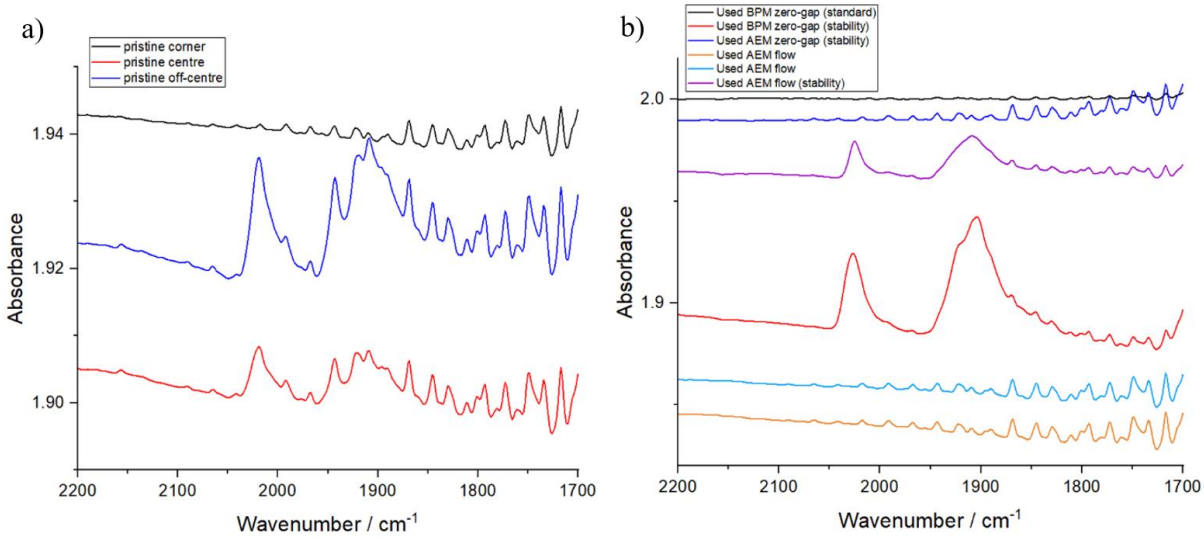

Figure S3: ATR-FTIR of GDE prepared using Mnbpy with MWCNT on carbon substrate paper, pre- (a) and post- (b) electrolysis.

FTIR spectra of the Mnbpy GDEs has been recorded before (figure S3a) and after electrolysis (figure S3b) at -0.98 V_{RHE}, for 6 hours in the 0.5 M $KHCO_3$ flow cell. Prior to the electrolysis the Mnbpy GDE shows ν(CO) bands that are assignable to [Mn(bpy)$(CO)_3$Br] (previously reported at 2027, 1937 and 1921 cm^{-1}) and [Mn(bpy)$(CO)_3(H_2O)]^+$ (previously reported at 2049, 1965 and 1953 cm^{-1}).[1] We find that the distribution of Mnbpy across the electrode is not even as a result of the hand painting method used here. Post-electrolysis, we do not see any evidence for additional metal carbonyl stretches which would be indicative of the complex degrading. However as with the pre-electrolysis electrode there is an uneven distribution of the complex across the GDE.

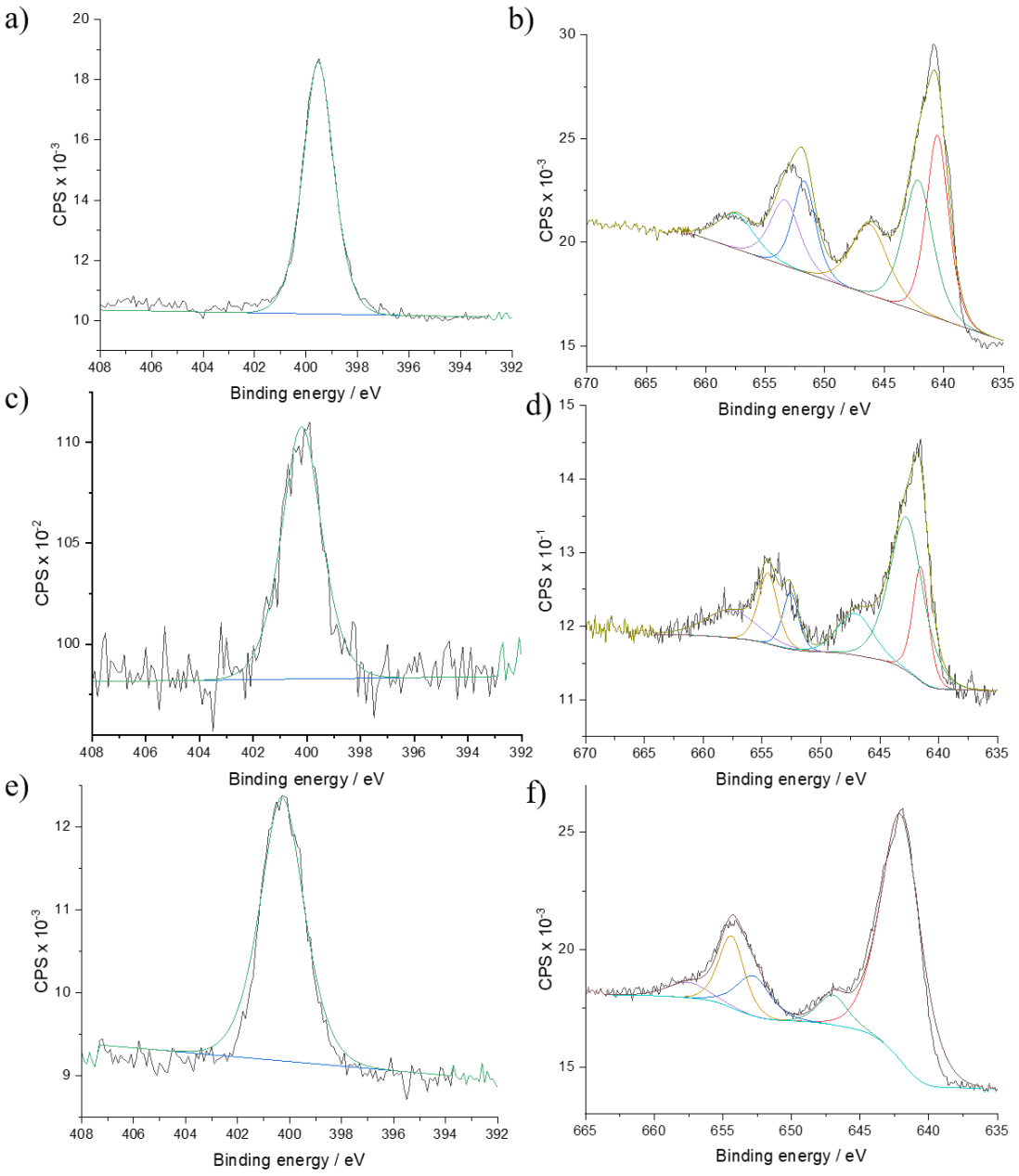

Figure S4: XPS of Mn(2,2'-bipyridine)(CO)$_3$Br powder N1s peak (a) and Mn2p peaks (b) and Mn(2,2'-bipyridine)(CO)$_3$Br on MWCNT immobilised on GDE structure with N1s peak and Mn2p peaks, respectively, pre- (c,d) and post-electrolysis (e,f).

In the text we report Mn 2p peaks of 641.5 eV and 647.1 eV. Additional peaks at 654.5 eV and 657.7 eV are proposed to be due to a mix of [Mn(bpy)(CO)$_3$Br] and [Mn(bpy)(CO)$_3$(solvent)] being present. The FTIR spectra and XPS analysis indicate that the Mn complex that is retained post-electrolysis is still primarily in the form of a mixture of [Mn(bpy)(CO)$_3$Br] and [Mn(bpy)(CO)$_3$(solvent)].

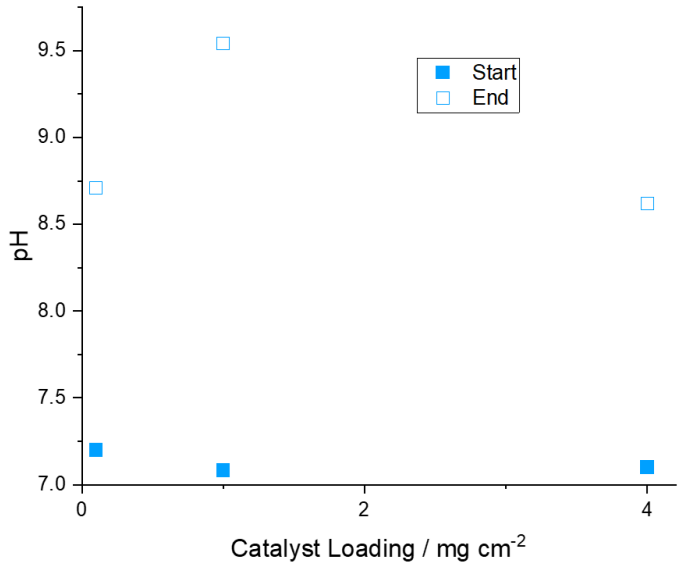

Figure S5: Catholyte pH before (solid) and after (hollow) CO_2 reduction by [Mn(bpy)(CO)$_3$Br] + MWCNT electrodes in 0.5 M $KHCO_3$ (aq) for 90 mins at -20 mA cm^{-2}.

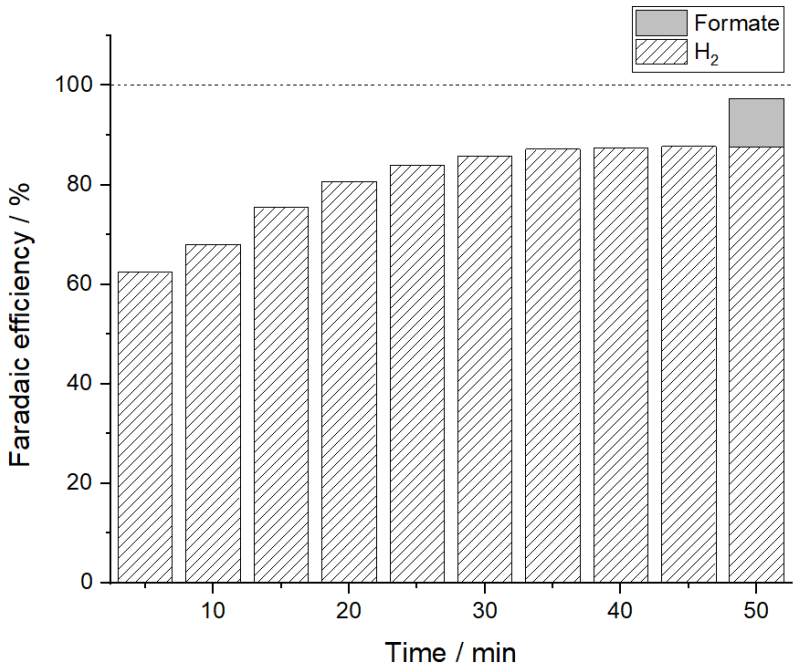

Figure S6: Electrochemical reduction under CO_2 atmosphere using electrode prepared with MWCNT at constant current of -20 mA cm^{-2} with 0.5 M $KHCO_3$ (aq), Selemion membrane, RuO_2 anode catalyst

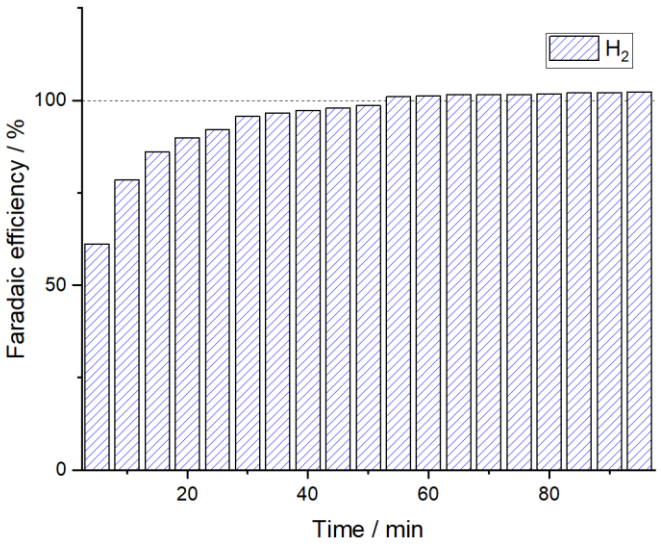

*Figure S7: Electrochemical reduction under N_2 atmosphere using electrode prepared with [Mn(bpy)(CO)$_3$Br]**(1)** and MWCNT at constant potential -0.98 V_{RHE} with 0.5 M $KHCO_3$ (aq), Selemion membrane, RuO_2 anode catalyst.*

In several experiments the total FE is below 100% even after formate crossover to the anode is accounted for. We also noted that the FE increased with time. Control experiments under N_2 (figure S7) show that the rise in FE is not unique to experiments under CO_2 and we propose that the initial low FE is due to competitive O_2 reduction. The FE is noted to be lower when experiments are carried out at more positive potentials (and hence lower current densities e.g. as in figure 3). In this case O_2 reduction will lead to a disproportionate drop in FE at low current densities. We also are operating at close to the detection limit of the GC system used in the low current density experiment and this may be a 2nd cause of the FE of < 100%. The experimental set-up was leak checked extensively and flow rate measured before and after the cell to account for any leaks so we do not believe this is the cause of the lower FE at low current densities.

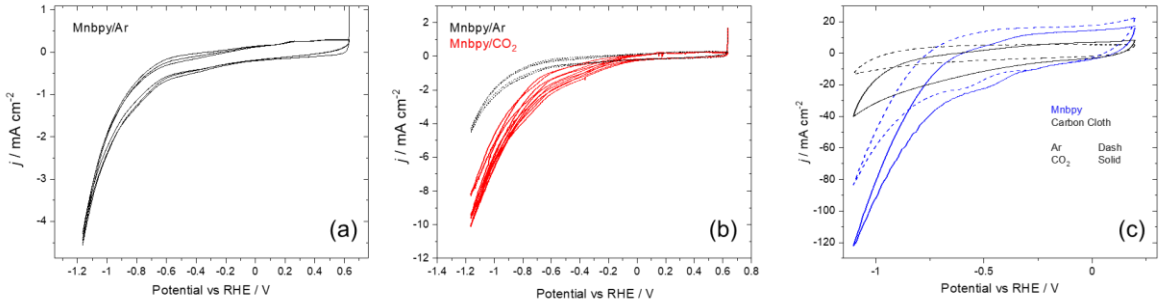

Figure S8: Cyclic voltammetry (CV) measurements of Mnbpy GDE suspended in a 0.5 M $KHCO_3$ (aq) electrolyte in a conventional 3 electrode measurement. Mnbpy electrode under Ar (a) and CO_2 (red, b) recorded at 5 mV s^{-1} following an initial conditioning at -0.1 V for 20 minutes. The response of the unmodified GDE support (carbon cloth, black) is compared to a Mnbpy GDE on the same support (blue) in CVs recorded at 200 mV s^{-1} (c).

To examine the potential dependence of the electrochemical response of the GDE we recorded cyclic voltammograms (CVs) of the Mnbpy GDE immersed in a 0.5 $KHCO_3$ electrolyte, figure S8. Under an Ar atmosphere the Mnbpy GDE shows a reduction at -0.6 V_{RHE}. This reduction is not present on the GDE without Mnbpy, figure S8c. The behaviour of Mnbpy has been extensively studied in solution[2] and when immobilised and this reduction is assigned to $[Mn^{I}(bpy)(CO)_3Br]$. Past studies indicate that the $[Mn(bpy)(CO)_3]^-$ is formed around *ca.* -0.8 V_{RHE}.[1] At low (5 mV s^{-1}) and higher scan rates (200 mV s^{-1}) we see an increase in current at this potential under Ar and CO_2 around *ca.* -0.7 to -0.8 V. $[Mn(bpy)(CO)_3]^-$ is proposed to be catalytically active for CO_2 reduction and it has also been reported that in aqueous solutions hydrogen production can occur from $[Mn(bpy)(CO)_3]^-$ when CO_2 is not present, in-line with the CVs in figure S8 at this potential.[1,3] At potentials negative of -0.78 V_{RHE} we also see the onset of CO_2 reduction in the flow cell. Therefore, we assign $[Mn(bpy)(CO)_3]^-$ on the GDE to be the catalytically active species for CO_2 reduction to CO in this study.

.

COMSOL modelling details

The simulation was a constant-current model, with 1-D geometry representing a porous catalyst layer (CL) and the diffusion layer of the electrolyte at the CL surface, following a reported reaction-diffusion model[4], with extension from a flat, solid electrode to a porous catalyst layer with CO_2 fed from a gas diffusion layer. [5,6]

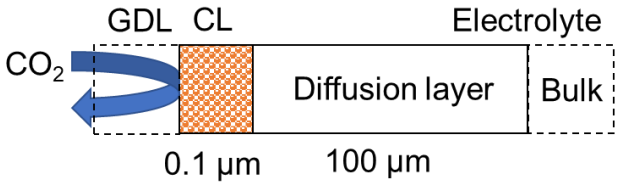

Four chemical species were considered (CO_2(aq), OH^-, HCO_3^-, and CO_3^{2-}).

Homogeneous reactions

In the liquid phase, both in the diffusion layer and in the liquid volume in the CL, the following 2 reactions are considered:

Reaction	**Forward rate constant**	**Backward rate constant**
R1: CO_2(aq) + OH^- ↔ HCO_3^-	5.93 m^3 mol^{-1} s^{-1}	1.34×10^{-4} s^{-1}
R2 HCO_3^- + OH^- ↔ CO_3^{2-} + H_2O	1.0×10^5 m^3 mol^{-1} s^{-1}	2.15×10^4 s^{-1}

Electrode reactions

Within the CL, the consumption of CO_2(aq),

$$R3 = -\frac{J}{2F}(FE_{CO})\frac{\varepsilon}{d}$$

and production of OH^- occurs as follows:

$$R4 = \frac{J}{F}\frac{\varepsilon}{d}$$

where J is the current density, F is Faraday's constant, FE_{CO} is the Faradaic efficiency for CO, ε is the catalyst layer porosity, and d is the catalyst layer thickness.

Governing equations

The time-dependent equations describing the concentrations of the species involving diffusion and reaction are as follows, assuming migration was negligible as there is a large concentration of supporting electrolyte.

$$\frac{\partial[CO_2(aq)]}{\partial t} = D_{CO2}\frac{\partial^2[CO_2(aq)]}{\partial x^2} - R1_f + R1_b + R3$$

$$\frac{\partial[OH^-]}{\partial t} = D_{OH-}\frac{\partial^2[OH^-]}{\partial x^2} - R1_f + R1_b - R2_f + R2_b + R4$$

$$\frac{\partial[HCO_3^-]}{\partial t} = D_{HCO3-}\frac{\partial^2[HCO_3^-]}{\partial x^2} + R1_f - R1_b + R2_f - R2_b$$

$$\frac{\partial[CO_3^{2-}]}{\partial t} = D_{CO_3^{2-}}\frac{\partial^2[CO_3^{2-}]}{\partial x^2} + R2_f - R2_b$$

D refers to the diffusion coefficient of each species, the f subscript refers to the forward reaction rate, the b subscript refers to the backward reaction rate, and R3 and R4 are set to 0 outside the CL.

Boundary conditions

At the boundary between the diffusion layer and the well-mixed bulk, all species were set to the initial bulk values. At the boundary between the CL and GDL, all species were set to zero flux, and CO_2(aq) was set to the maximum CO_2 solubility.

Diffusion coefficients

Species	**Diffusion coefficient / m^2 s^{-1}**
CO_2(aq)	1.91×10^{-9}
OH^-	5.27×10^{-9}
HCO_3^-	9.23×10^{-10}
CO_3^{2-}	1.19×10^{-9}

Other parameters

Parameter	**Value**	**Units**
Bulk HCO_3^- concentration	0.5	M
Faradaic efficiency for CO	50	%
Catalyst layer porosity	0.6	-

The simulation was conducted in COMSOL 5.0 using the Coefficient Form PDE interface, and the pH at the junction of the CL and the diffusion layer (i.e. the outermost surface of the CL) is reported after reaching steady state (20 s).

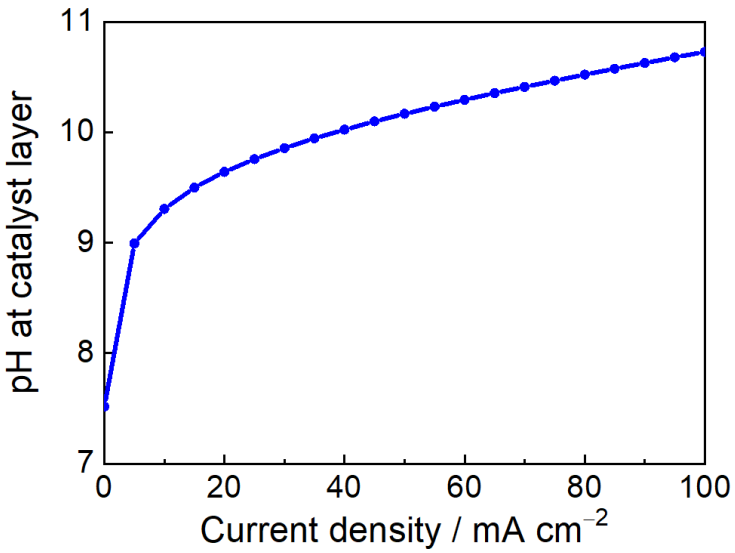

Figure S9: COMSOL simulations into the effect of changing current densities on pH at the catalyst layer.

Paper	Catalyst	Cell Design	Electrolyte	Max partial Current densities for CO / mA cm^{-2}	Potential Applied vs RHE / V	Max FE_{CO} / %
Nervi, Chem. Commun., 2019[7]	*fac*-Mn(apbpy)$(CO)_3$Br	H-type	0.1 M $KHCO_3$ (aq)	5	-0.96	60
Nervi, Chem Eng Journal, 2021[8]	*fac*-Mn(apbpy)$(CO)_3$Br	Flow	0.2 M $KHCO_3$ (aq)	6	-0.67	97
Reuillard, JACS, 2017[9]	[MnBr(2,2′-bipyridine)$(CO)_3$]	H-type	0.5 M $KHCO_3$ (aq)	0.3	-0.66	34
Walsh, Organometallics, 2019[10]	[Mn(bpy-$(COOH)_2$)$(CO)_3$Br]	Mercury pool	0.1 M KCl, 0.5 M K_2CO_3 (aq)	2.3	-0.76	65
Walsh, Chem. Commun., 2014[1]	*fac*-Mn(apbpy)$(CO)_3$Br	Single compartment	30 mM Na_2HPO_4, 30 mM NaH_2PO_4 (aq)	3	-0.76	51
Walsh, Faraday Discuss, 2015[3]	[Mn(bpy)$(CO)_3$Br] and [Mn(bpy(tBu)$_2$)$(CO)_3$Br]	H-type	0.1 M phosphate buffer (aq)	1.8	-0.74	89
Smith, Sustainable Energy Fuels, 2019[11]	*fac*-Mn(apbpy)$(CO)_3$Br	Single compartment	60 mM phosphate buffer (aq)	4	-0.96	0.43
Sato, ACS Catalysis, 2018[12]	[Mn{4,4'-di(1H-pyrrolyl-3-propyl carbonate)-2,2'-bipyridine}$(CO)_3$MeCN]$^+(PF_6)^-$	Single compartment	0.1 M $K_2B_4O_7$, 0.2 M K_2SO_4 (aq)	2	-0.39	81.4
This work	[MnBr(2,2′-bipyridine)$(CO)_3$]	Flow	0.5 M $KHCO_3$ (aq)	14	-0.98	63
This work	[MnBr(2,2′-bipyridine)$(CO)_3$]	Zero-gap, reverse bias BPM	1 M KOH (aq)	35.1	-3.27 (two-electrode measurement)	70.2

Table S1: State of the art Mn based catalysts for CO_2 electroreduction in aqueous solvents.

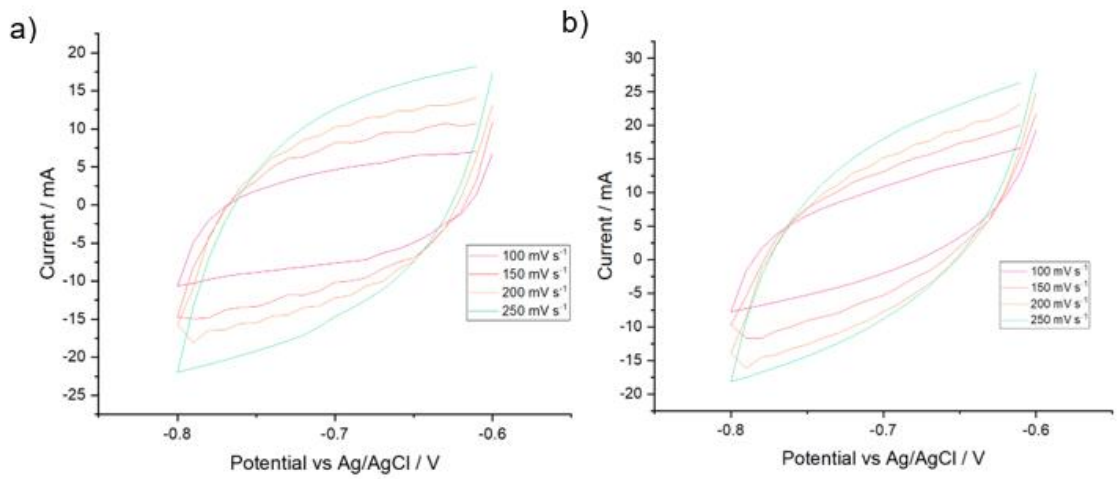

Figure S10: CVs of [Mn(bpy)(CO)$_3$Br] + MWCNT electrode pre- (a) and post-electrolysis (b) with Pt counter and Ag/AgCl reference electrodes in 0.5 M $KHCO_3$ at 100 mV s^{-1} (pink), 150 mV s^{-1} (orange), 200 mV s^{-1} (yellow) and 250 mV s^{-1} (green).

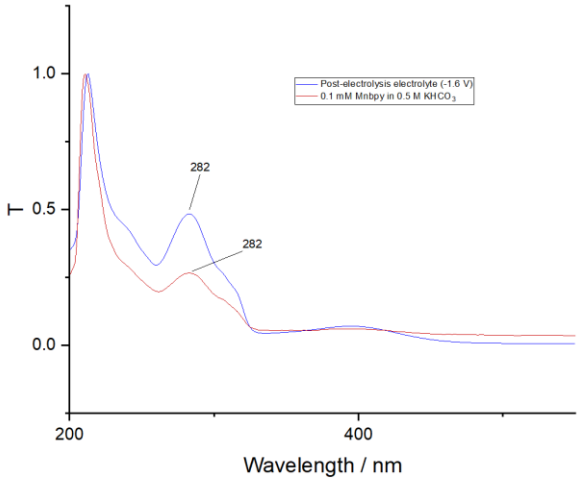

Figure S11: UV/vis spectrometry of 0.5 M $KHCO_3$ (aq) after electrolysis using an electrode with [Mn(bpy)(CO)$_3$Br] + MWCNT (blue) and 0.5 M $KHCO_3$ (aq) with 0.1 mM [Mn(bpy)(CO)$_3$Br] left in light for 1 minute (red).

Concentration calculations of Mnbpy can be carried out by comparison to the spectrum of a known concentration in the aqueous electrolyte. However these should be treated with some caution due to the potential for concentration dependent aggregation in water but they do provide an estimate of [Mn(bpy)(CO)$_3$Br] in the electrolyte which post electrolysis is 15% of the catalyst originally deposited.

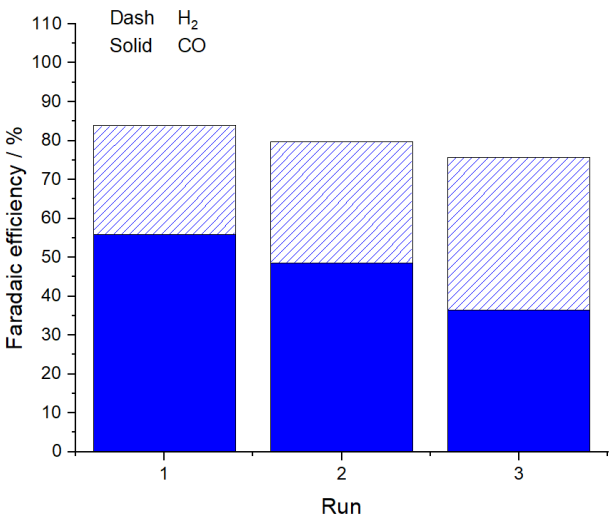

Figure S12: Electrochemical CO_2 reduction by Mnbpy when 4 mg cm^{-2} Mnbpy loading is used with a 0.5 M $KHCO_3$ (aq) electrolyte at -0.98 V_{RHE} where Run1 uses fresh electrolyte, Run2 reuses this electrolyte after a 30-minute catalyst recovery period and Run3 replaces the electrolyte with fresh electrolyte.

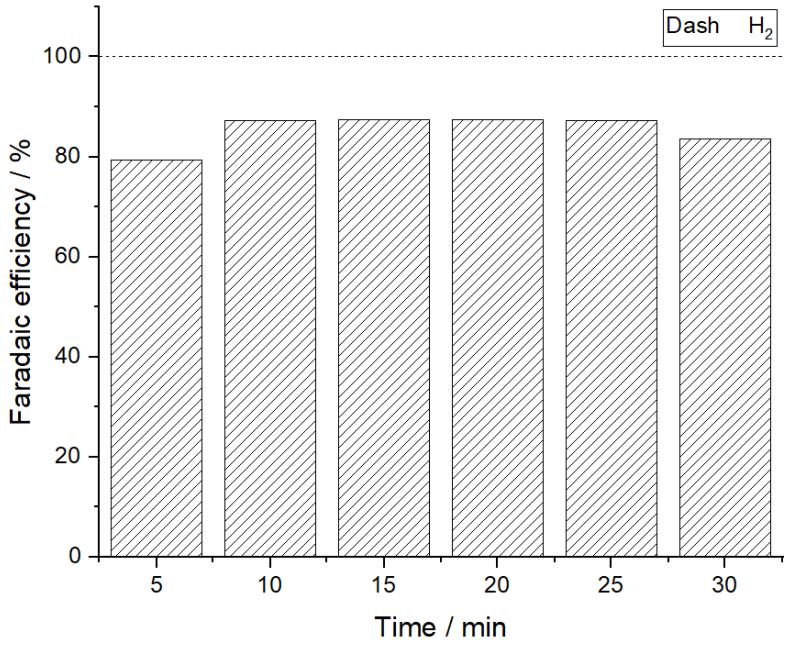

Figure S13: Electrochemical reduction under CO_2 atmosphere using electrode prepared with MWCNT at constant potential -0.98 V_{RHE} with 0.5 M $KHCO_3$ (aq) spiked with 4 mg [Mn(bpy)$(CO)_3$Br], Selemion membrane, RuO_2 anode catalyst.

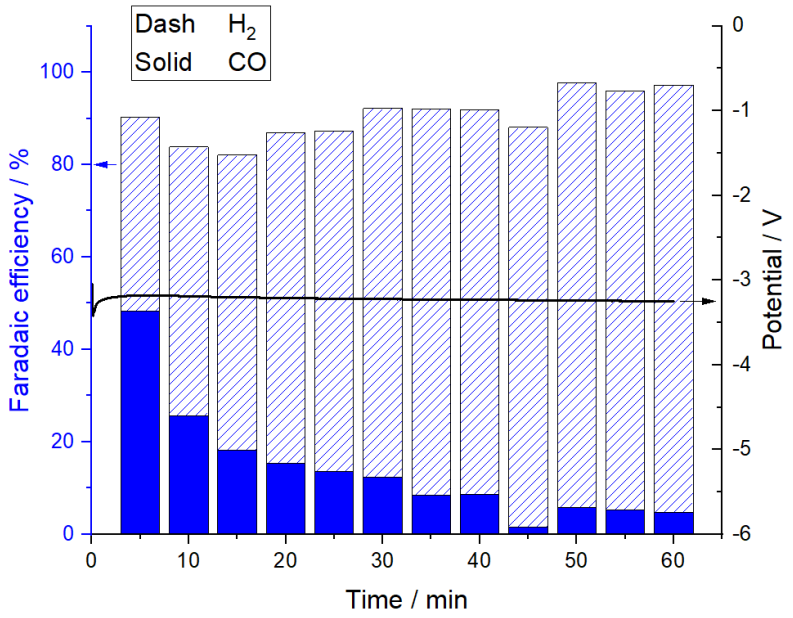

Figure S14: Mnbpy/MWCNT in zero-gap system using AEM (Sustainion) at 20 mA cm^{-2} using 1M KOH (aq) anolyte.

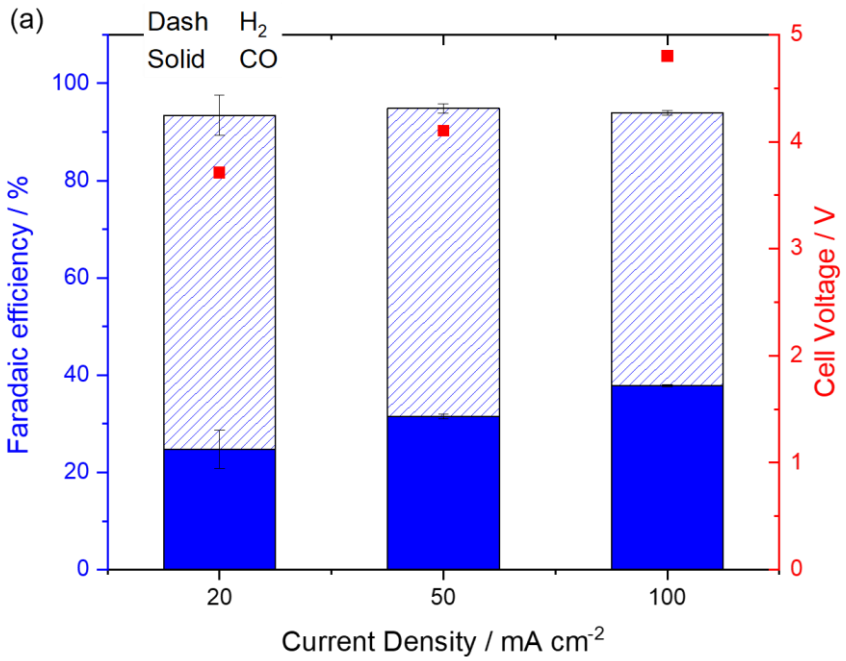

Figure S15: Ag in a reverse biased BPM zero-gap electrolyser at -20, -50 and -100 mA cm^{-2} for ten minutes using a 1M KOH anolyte. The increase in FE for CO with current density is in-line with previous experiments[13] *with Ag electrodes in a reverse biased BPM where we assigned the higher selectivity to the increase in local pH due to higher H^+consumption rates.*

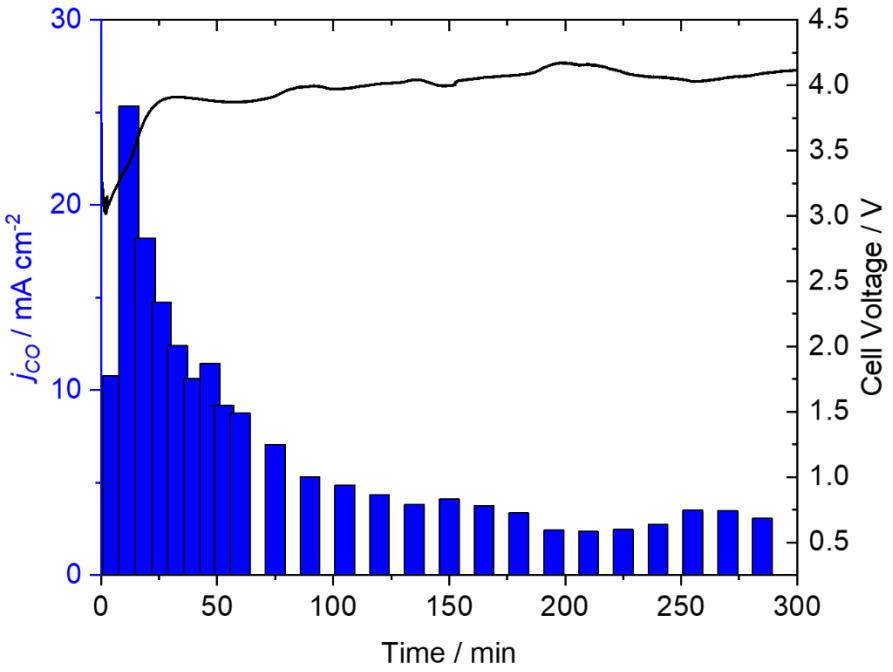

Figure S16: Mnbpy/MWCNT in a reverse biased BPM zero-gap electrolyser at -50 mA cm^{-2} for 5 hours using a 1M KOH anolyte.

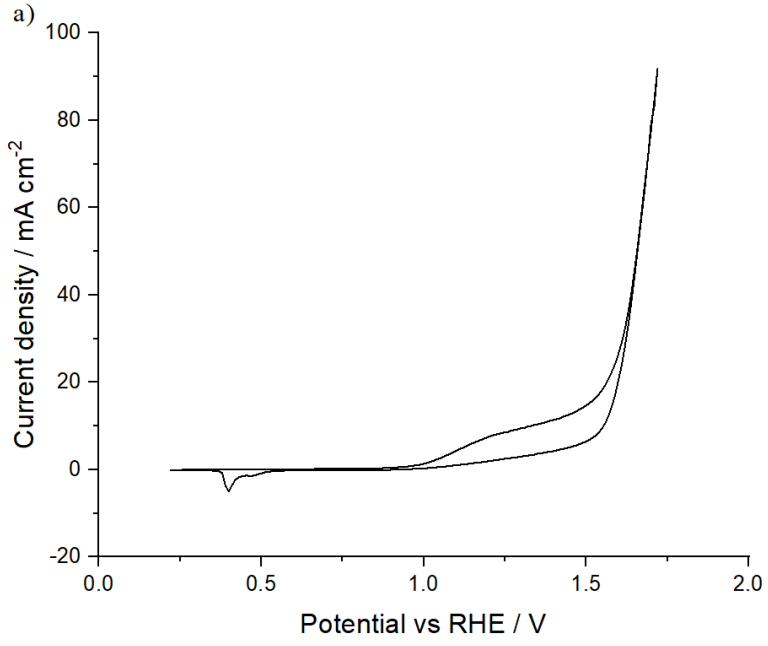

Figure S17: CV of RuO_2/Nafion removed from the anode post experiment and drop-cast (Nafion support) onto Au disc electrode in 1 M H_2SO_4 (aq) with Pt mesh (counter) and Ag/AgCl (reference) at scan rate 100 mV s^{-1}. RuO_2 recovered from coated titanium anode post-electrolysis. The RuO_2 (~6 mg) was prepared in a mixture of IPA and water and Nafion solution. The resulting ink was sonicated for

30 minutes and dropped in 10 µL portions onto a Au disc electrode, which was allowed to dry overnight.[14]

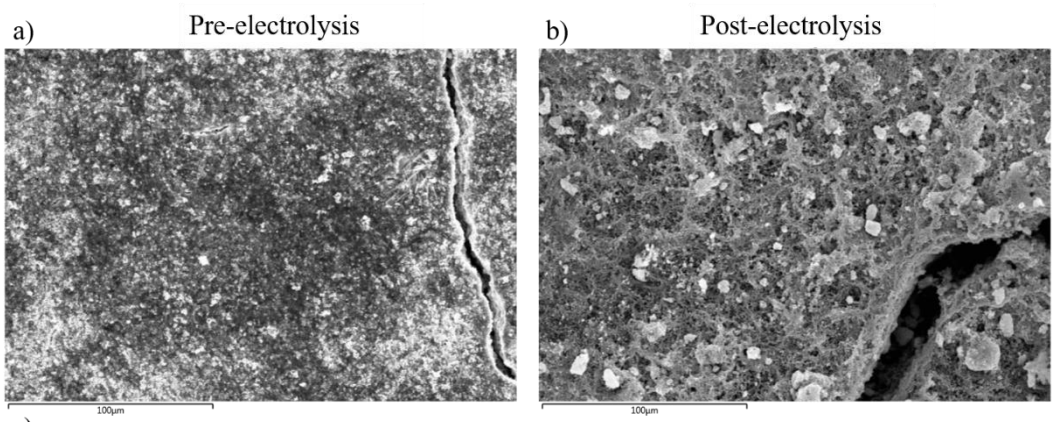

c)

	atomic %				
	F	Ru	K	Br	Ru/F
Pristine	54.46	45.54	0	0	0.836
Used	69.86	28.2	1.69	0.25	0.404

Figure S18: SEM (a,b) and EDX-mapping (c) of anode prepared using RuO_2 with Nafion on carbon paper, pre- and post-electrolysis at -50 mA cm^{-2} in a zero-gap cell.

References

1 J. J. Walsh, G. Neri, C. L. Smith and A. J. Cowan, *Chemical Communications*, 2014, **50**, 12698–12701.

2 M. Bourrez, F. Molton, S. Chardon-Noblat and A. Deronzier, *Angewandte Chemie - International Edition*, 2011, **50**, 9903–9906.

3 J. J. Walsh, C. L. Smith, G. Neri, G. F. S. Whitehead, C. M. Robertson and A. J. Cowan, *Faraday Discussions*, 2015, **183**, 147–160.

4 N. Gupta, M. Gattrell and B. MacDougall, *Journal of Applied Electrochemistry*, 2006, **36**, 161–172.

5 T. Burdyny and W. A. Smith, *Energy and Environmental Science*, 2019, **12**, 1442–1453.

6 K. Xie, R. K. Miao, A. Ozden, S. Liu, Z. Chen, C.-T. Dinh, J. E. Huang, Q. Xu, C. M. Gabardo, G. Lee, J. P. Edwards, C. P. O'Brien, S. W. Boettcher, D. Sinton and E. H. Sargent, *Nature Communications*, 2022, **13**, 3609.

7 L. Rotundo, J. Filippi, R. Gobetto, H. A. Miller, R. Rocca, C. Nervi and F. Vizza, *Chemical Communications*, 2019, **55**, 775–777.

8 J. Filippi, L. Rotundo, R. Gobetto, H. A. Miller, C. Nervi, A. Lavacchi and F. Vizza, *Chemical Engineering Journal*, 2021, **416**, 129050.

9 B. Reuillard, K. H. Ly, T. E. Rosser, M. F. Kuehnel, I. Zebger and E. Reisner, *Journal of the American Chemical Society*, 2017, **139**, 14425–14435.

10 J. J. Walsh, G. Neri, C. L. Smith and A. J. Cowan, *Organometallics*, 2019, **38**, 1224–1229.

11 C. L. Smith, R. Clowes, R. S. Sprick, A. I. Cooper and A. J. Cowan, *Sustainable Energy and Fuels*, 2019, **3**, 2990–2994.

12 S. Sato, K. Saita, K. Sekizawa, S. Maeda and T. Morikawa, *ACS Catalysis*, 2018, **8**, 4452–4458.

13 B. Siritanaratkul, M. Forster, F. Greenwell, P. K. Sharma, E. H. Yu and A. J. Cowan, *Journal of the American Chemical Society*, 2022, **144**, 7551–7556.

14 S. Chalupczok, P. Kurzweil, H. Hartmann and C. Schell, *International Journal of Electrochemistry*, 2018, **2018**, 1–15.